

Chapter 1

THE MILKY WAY AS MODELED BY PERCOLATION AND SUPERBUBBLES

Lorenzo Zaninetti *

Physics Department, via P.Giuria 1,
I-10125 Turin, Italy

PACS 98.35.-a ; 98.38.Mz **Keywords:** Characteristics and properties of the Milky Way galaxy; Supernova remnants

Abstract

The spiral structure of the Milky Way can be simulated by adopting percolation theory, where the active zones are produced by the evolution of many supernova (SN). Here we assume conversely that the percolative process is triggered by superbubbles (SB), the result of multiple SNs. A first thermal model takes into account a bursting phase which evolves in a medium with constant density, and a subsequent adiabatic expansion which evolves in a medium with decreasing density along the galactic height. A second cold model follows the evolution of an SB in an auto-gravitating medium in the framework of the momentum conservation in a thin layer. Both the thermal and cold models are compared with the results of numerical hydro-dynamics. A simulation of GW 46.4+5.5, the Gould Belt, and the

*Email address: zaninetti@ph.unito.it

Galactic Plane is reported. An elementary theory of the image, which allows reproducing the hole visible at the center of the observed SB, is provided.

1. Introduction

The term supershell was observationally defined by [1], where eleven HI objects were examined. Supershells have been observed as expanding shells, or holes, in the HI-column density distribution of our galaxy, in the Magellanic Clouds, in the dwarf irregular galaxy Ho-II [2], and in the nearby dwarf galaxy IC 2574 [3]. The dimensions of these objects span from 100 pc to 1700 pc and often present elliptical shapes or elongated features, which are difficult to explain based on an expansion in a uniform medium. These structures are commonly explained through introducing theoretical objects named bubbles or superbubbles (SB); these are created by mechanical energy input from stars (see for example [4]; [5]). Thus, the origin of a supershell is not necessarily an SB, and other possible origins include collisions of high-velocity clouds (see for example [6]; [7]). A worm is another observed feature that may, or may not, be associated with a wall of an SB. Galactic worms were first identified as irregular, vertical columns of atomic gas stretching from the galactic plane; now, similar structures are found in radio continuum and infrared maps (see for example [8]). SBs are also observed in other galaxies, we cite two examples among many: a kinematical and photometric catalog was compiled for 210 H II regions in the Large Magellanic Cloud [9] and 12 SBs were classified in the irregular galaxy NGC 1569 [10].

The models that explain SBs as being due to the combined explosions of supernova in a cluster of massive stars are now briefly reviewed. Semi-analytical and hydrodynamical calculations are generally adopted. In semi-analytical calculations, the thin-shell approximation can be the key to obtaining the expansion of the SB; see, for example, [11, 12, 13, 14, 15].

The thin-shell approximation has already been used in a variety of different problems, and with both analytical and numerical approaches (besides the review by [16], see [17] and [18]). Thus the validity and limitations of the method are well known. For instance, modeling is fast and simple because the shell dynamics are only included in an approximate way, while the fluid variables are not included at all. The price that one has to pay is a lack of knowledge of the density and velocity profiles and, obviously, neither the onset and development of turbulence, instabilities, or mixing can be followed. These facts limit the applications of this method to deriving only the general shapes, approximate expansion rates, and gross features of the surface mass-density distributions of the shells.

The hydro-dynamical approximation was used by [19]. As for the effect of magnetic fields, a semi-analytical method was introduced by [20] and a magneto-hydrodynamic code has been adopted by various authors [21, 22, 23]. The often adopted exponential and vertical profiles in density do not correspond to a physical process of equilibrium. The case of an isothermal self-gravitating disk (ISD) is an equilibrium vertical profile which can be coupled with momentum conservation. The models cited leave some questions unanswered or only partially answered:

- Is it possible to calibrate the vertical profile of an ISD?

- Is it possible to deduce an analytical formula for the temporal evolution of an SB in the presence of a vertical profile density as given by an ISD?
- Is it possible to deduce numerical results for an SB when the expansion starts at a given galactic height?
- What is the influence of galactic rotation on the temporal evolution of an SB?
- Can we explain the worms as a particular effect using image theory applied to SBs?

In order to answer these questions, Section 2. reviews the percolation theory which allows modeling a spiral galaxy. Section 3. introduces a numerical code which solves the momentum equation coupled with the variation of pressure in the presence of the injection of mechanical luminosity and the adiabatic losses, the so called *thermal model*. Section 4. models an aspherical expansion, in a vertical profile in the number of particles as given by an ISD, the so called *cold model*. Section 5. reports a comparison between the numerical hydro-dynamical calculations and the two codes here presented. Section 6. models the SBs associated with GW 46.4+5.5, the Gould Belt, and the Galactic Plane. Section 7. contains detailed information on how to build an image of an SB both in the symmetric and asymmetric case.

2. The Percolation

The appearance of arms can be simulated through percolation theory [24, 25, 26, 27, 28]. The fundamental hypotheses and the parameters adopted in the simulation will now be reviewed.

1. The motion of a gas on the galactic plane has a constant rotational velocity, denoted by V_G (in the case of spiral type Sb 218 km s^{-1}). Here the velocity, V_G , is expressed in units of 200 km s^{-1} and will therefore be $V_G = 1.09$.
2. The polar simulation array made by rings and cells has a radius $R_G = 12 \text{ kpc}$. The number of rings, (59), by the multiplication of R_G with the number of rings for each kpc, denoted by $n_{\text{ring/kpc}}$, which in our case is 5. Every ring is then made up of many *cells*, each one with a size on the order of the galactic thickness, $\approx 0.2 \text{ kpc}$. The parameter $n_{\text{ring/kpc}}$ can also be found by dividing 1 kpc by the cell's approximate size.
3. The global number of cells, 11121, multiplied by the probability of spontaneous new cluster formation, p_{sp} (for example 0.01), allows the process to start (with the previous parameters, 111 new clusters were generated). Each one of these sources has six new surroundings that are labeled for each ring.
4. In order to better simulate the decrease of the gas density along the radius, a stimulated probability of forming new clusters with a linear dependence by the radius, $p_{\text{st}} = a + bR$, was chosen. The values a and b are found by fixing p_{rmax} (for example 0.18), the stimulated probability at the outer ring, and p_{rmin} (for example 0.24) in the inner ring; of course, $p_{\text{rmin}} \geq p_{\text{rmax}}$. This approach is surprisingly similar to

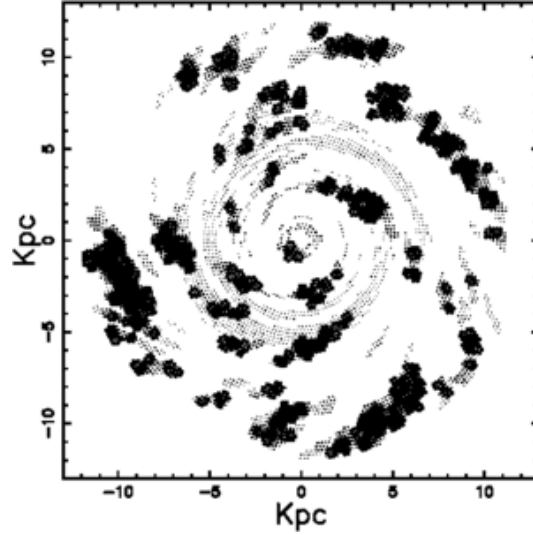


Figure 1. A typical simulation of the galaxy's arms. Here 'active' is the final number of active cells, 'random' the initial number of randomly distributed sources, 'pc' the considered probability, 'cells' the total number of cells, R the radius in Kpc, 'ring/kpc' the number of rings considered per kpc, the size of the cells is in kpc, v the velocity in units of 200 Km/sec, and the time is expressed in units of millions of years, see the numerical values in Table 1

the introduction of an anisotropic probability distribution in order to better simulate certain classes of spirals [29].

5. Now, new sources are selected in each ring based on the hypothesis of different stimulated probabilities. A rotation curve is imposed so that the array rotates in the same manner as the galaxy. The procedure repeats itself n times (100); we denote by t_G the age of the simulation, viz., $100 \cdot 10^7$ yr, where 10^7 yr is the astrophysical counterpart of one time step.
6. In order to prevent catastrophic growth, the process is stopped when the number of surroundings is greater than max (1000) and restarts by spontaneous probability.
7. The final number of active cells (3824) is plotted with the size, which decreases linearly with the cluster age. In other words, the young clusters are bigger than the old ones. Only ten cluster ages are shown; only cells with an age of less than life (in our case $10 \cdot 10^7$ yr) are selected. A more deterministic approach has been followed by [30], where a model that connects the energy injection by star formation with the resulting interstellar structures in a differentially rotating disc has been introduced.

A typical run is shown in Figure 2. and in Table 1 we summarize the parameters used in this simulation.

A real spiral galaxy as observed in the infrared is reported in Figure 2 as observed by the Spitzer Space Telescope, more details are available at <http://www.spitzer.>

Table 1. Parameters of the model

<i>galactic radius</i>	$12kpc$
<i>rings/kpc</i>	5
<i>stochastic probability</i>	0.01
<i>timestep</i>	$10^7 years$
<i>cells</i>	11121
<i>active</i>	3894



Figure 2. Composite image in the infrared of M100.

caltech.edu/.

3. The thermal model for SBs

The starting equation for the evolution of the SB [11, 12, 31] is momentum conservation applied to a pyramidal section, characterized by a solid angle $\Delta\Omega_j$:

$$\frac{d}{dt} (\Delta M_j \dot{R}_j) = p R_j^2 \Delta\Omega_j \quad , \quad (1)$$

where the pressure of the surrounding medium is assumed to be negligible and the mass is confined in a thin shell with mass ΔM_j . The subscript j was added here in order to note that this is not a spherically symmetric system. Due to the fact that p is uniform in the cavity of the SB, a summation to obtain the total volume, such as

$$V = \sum \Delta\Omega_j R_j^3 / 3 \quad , \quad (2)$$

is necessary to determine its value. The mass conservation equation for a thin shell is

$$\Delta M_j = \frac{1}{3} R_j^3 \bar{\rho}_j \Delta \Omega_j \quad . \quad (3)$$

The pressure is enclosed in the energy conservation equation,

$$\frac{1}{\gamma - 1} \frac{d(pV)}{dt} = L - p \frac{dV}{dt} \quad , \quad (4)$$

where $L = E_0 R_{\text{SN}} / 4\pi$ denotes the mechanical luminosity injected into a unit solid angle and $\gamma = 5/3$. Equation (4) can be expanded, obtaining

$$\frac{dp}{dt} = \frac{L(\gamma - 1)}{V} - \gamma \frac{p}{V} \frac{dV}{dt} \quad . \quad (5)$$

Formulae (1) and (5) will be our basic equations to numerically integrate in the bursting phase. An approximation concerning the pressure can be obtained by ignoring the second term of the rhs in (4); this leads to

$$p = \frac{2E_0 R_{\text{SN}} t}{3V} \quad , \quad (6)$$

where t is the considered time, R_{SN} the rate of supernova explosions, E_0 the energy of each supernova, and V is computed as in Equation (2). On continuing to consider the case of constant density, the volume becomes

$$V = \frac{4\pi}{3} R^3 \quad . \quad (7)$$

Equations (1) and (6) lead to

$$\frac{d}{dt} (\bar{\rho} R^3 \dot{R}) = \frac{3E_0 R_{\text{SN}}}{2\pi} \frac{t}{R} \quad . \quad (8)$$

In order to integrate the above equation, $R^3 \dot{R} = AR^\alpha$ is imposed. After adopting the initial condition of $R = 0$ at $t = 0$ and assuming $\bar{\rho}$ is constant irrespective of R or t , the equation for the expansion speed is obtained:

$$\dot{R} = \frac{\alpha + 1}{\alpha} \frac{3E_0 R_{\text{SN}}}{4\pi \bar{\rho} R^4} t^2 \quad . \quad (9)$$

By integrating the previous equation, “the expansion law” is obtained:

$$R = \left[\frac{5(\alpha + 1)}{4\pi\alpha} \right]^{1/5} \left(\frac{E_0 R_{\text{SN}}}{\bar{\rho}} \right)^{1/5} t^{3/5}, \quad (10)$$

which is identical to equation (10.34) of [11], since $\alpha = 7/3$.

3.1. After SN Bursts Stop

It is clear that an upper limit should be inserted into the basic equation (6); this is the time after which the bursting phenomenon stops, t^{burst} .

Since there is a pdV term in the the First Law of Thermodynamics ($dQ = 0 = dU + pdV$), the total thermal energy decreases with time. The pressure of the internal gas decreases according to the adiabatic law,

$$p = p_1 \left(\frac{V_1}{V} \right)^{5/3} , \quad (11)$$

where

$$p_1 = \frac{2}{3} \frac{E_0 R_{\text{SN}} t^{\text{burst}}}{V_1} , \quad (12)$$

and the equation for the conservation of momentum becomes

$$\frac{d}{dt} \left(\bar{\rho}_j R_j^3 \dot{R}_j \right) = 3 \frac{p_1 V_1^{5/3}}{V^{5/3}} R_j^2 . \quad (13)$$

It is important to remember that this phase occurs after the SN burst stops. At that time ($t = t^{\text{burst}}$), the volume of the bubble is computed by using $R_j(t^{\text{burst}})$, and the expansion speed is equal to $\dot{R}_j(t^{\text{burst}})$, both of which are obtained from the numerical solution of Equation (8). On assuming (also here) that $\bar{\rho}$ is constant irrespective of R or t , Equation (12) is now inserted into Equation (1) and the expansion law is obtained for the after-burst phase,

$$R = \left(\frac{147}{4\pi} \right)^{1/7} \left(\frac{E_0 R_{\text{SN}} t^{\text{burst}} R_1^2}{\bar{\rho}} \right)^{1/7} t^{2/7} , \quad (14)$$

which is identical to equation (10.33) of [11].

3.2. Numerical Integration

The differential equations need to be solved by sectors, with each sector being treated as independent from the others, except for the coupling in computing the volume of the bubble, see Equation (2). The range of the polar angle θ (180°) will be divided into n_θ steps, and the range of the azimuthal angle ϕ (360°) into n_ϕ steps. This will yield $(n_\theta + 1)(n_\phi + 1)$ directions of motion that can also be identified with the number of vertices of the polyhedron representing the volume occupied by the expansion; this polyhedron varies from a sphere to various morphological shapes based on the swept up material in each direction. In 3D plots showing the expansion surface of the explosion, the number of vertices is $n_v = (n_\theta + 1)(n_\phi + 1)$ and the number of faces is $n_\theta \cdot n_\phi$, typically we have $n_\theta = 50$ and $n_\phi = 50$ (in this case the subscript varies between 1 and 2601). However, all calculated models are axisymmetric, and the essential number of points to draw such figures is only $n_\theta + 1 = 51$. R_{up} , R_{eq} and R_{down} are now introduced, which represent the distances from the position of the the OB associations (denoted by z_{OB}) to the top, to the left and to the bottom of the bubble.

3.3. The Numerical Equations

At each time step, Δt , the volume V of the expanding bubble is computed, see Equation (2). In other words, the volume V swept up from the explosions is no longer a sphere, but becomes an egg or an hourglass. The pressure in the first phase, see Equation (5), is computed through the following finite-difference approximation:

$$p^k = p^{k-1} + \left[L \frac{\gamma - 1}{V^k} - \gamma \frac{p^{k-1} V^k - V^{k-1}}{V^k \Delta t} \right] \Delta t \quad , \quad (15)$$

where k is the number of steps employed.

Equation (1) now leads to

$$\frac{d}{dt} (\bar{\rho}_j R_j^3 \dot{R}_j) = 3p R_j^2 \quad , \quad (16)$$

which may rewritten as

$$3R_j^2 \dot{R}_j^2 + R_j^3 \ddot{R}_j = 3p \frac{R_j^2}{\bar{\rho}_j} - \frac{\dot{\bar{\rho}}_j}{\bar{\rho}_j} R_j^3 \dot{R}_j \quad . \quad (17)$$

The first term represents the ram pressure of the stratified ISM on the expanding surface and the second represents the inertia of the bubble. The average density $\bar{\rho}_j$ is numerically computed according to the algorithm outlined in subsection 3.5.; the time derivative of $\bar{\rho}_j$ at each time step Δt is computed according to the finite difference-approximation,

$$\dot{\bar{\rho}}_j = \frac{\bar{\rho}_j^k - \bar{\rho}_j^{k-1}}{\Delta t} \quad , \quad (18)$$

where k is the number of steps considered.

Equation (17) can be re-expressed as two differential equations (along each direction j) of the first order suitable to be integrated:

$$\frac{dy_{1,j}}{dt} = y_{2,j} \quad , \quad (19)$$

$$\frac{dy_{2,j}}{dt} = 3p \frac{1}{\bar{\rho}_j y_{1,j}} - 3 \frac{y_{2,j}^2}{y_{1,j}} - \frac{\dot{\bar{\rho}}_j}{\bar{\rho}_j} y_{2,j} \quad . \quad (20)$$

In the new regime ($t \geq t^{\text{burst}}$), Equation (13) now becomes

$$3R_j^2 \dot{R}_j^2 + R_j^3 \ddot{R}_j = 3 \frac{p_1 V_1^{5/3}}{V^{5/3} \bar{\rho}_j} R_j^2 - \frac{\dot{\bar{\rho}}_j}{\bar{\rho}_j} R_j^3 \dot{R}_j \quad . \quad (21)$$

Equation (21) can be re-expressed as two differential equations (along each direction j) of the first order suitable to be integrated:

$$\frac{dy_{1,j}}{dt} = y_{2,j} \quad , \quad (22)$$

$$\frac{dy_{2,j}}{dt} = \frac{3p_1 V_1^{5/3}}{V^{5/3} \bar{\rho}_j y_{1,j}} - 3 \frac{y_{2,j}^2}{y_{1,j}} - \frac{\dot{\bar{\rho}}_j}{\bar{\rho}_j} y_{2,j} \quad . \quad (23)$$

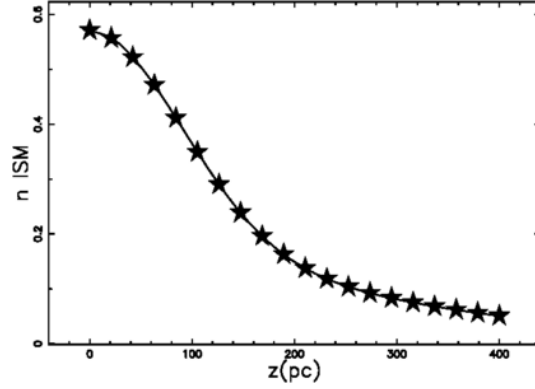


Figure 3. The average structure of the gaseous disk in the z -direction; z is allowed to vary between 0 pc and 400 pc.

The integrating scheme used is the Runge–Kutta method, and in particular the sub-routine RK4 ([32]); the time derivative of the density along a certain direction j , $\dot{\rho}_j$, is computed at each time step according to formula (18).

The integration time, t_{age} , and the time steps, are always indicated in the captions of the various diagrams. The pressure across the bursting time is continuous. This is because the first value of the pressure after the bursting time is that of the last step in the bursting phase, modified according to the adiabatic law modelled by formula (11).

The upper limit chosen to integrate the differential equations is $t_{\text{age}} = 2.5 \cdot 10^7$ yr; this is the approximate age of GSH 238.

3.4. The Density Profile

The vertical density distribution of galactic HI is well-known; specifically, it has the following three component behavior as a function of z , the distance from the galactic plane in pc:

$$n(z) = n_1 e^{-z^2/H_1^2} + n_2 e^{-z^2/H_2^2} + n_3 e^{-|z|/H_3}. \quad (24)$$

We took [33, 34, 35] $n_1=0.395$ particles cm^{-3} , $H_1=127$ pc, $n_2=0.107$ particles cm^{-3} , $H_2=318$ pc, $n_3=0.064$ particles cm^{-3} , and $H_3=403$ pc. This distribution of galactic HI is valid in the range $0.4 \leq R \leq R_0$, where $R_0 = 8.5$ kpc and R is the distance from the center of the galaxy. A plot showing such a dependence of the ISM density on z is shown in Figure 3.

3.5. Computation of the Swept Mass

The ISM density is not constant, but varies in the z -direction according to Equation (24). The swept mass can therefore be computed in a certain direction j using the following algorithm:

1. The pyramidal sector is divided into layers (for example 1000) whose radii range from $R_{L-1/2}$ to $R_{L+1/2}$.

2. In each layer the volume $\Delta V_L = \frac{1}{3}(R_{L+1/2}^3 - R_{L-1/2}^3)$ is computed as well as the corresponding mass, $\Delta M_L = \Delta V_L \rho_j (z = R_L \cos \theta_j + z_{\text{OB}})$, where θ_j represents an angle between the z -axis and the j th radial path.
3. The various contributions, ΔM_L , are added in order to obtain the total swept mass in the considered sector.
4. The average density along a sector j as $\bar{\rho}_j$ is calculated using ΔM_L and ΔV_L as $\bar{\rho}_j = \sum_L \Delta M_L / \sum_L \Delta V_L$.

3.6. Astrophysical Units

Our basic units are: time (t_7), which is expressed in units of 10^7 yr; E_{51} , the energy in 10^{51} erg; n_0 , the density expressed in particles cm^{-3} (density $\rho_0 = n_0 m$, where $m=1.4m_{\text{H}}$); and N^* , which is the number of SN explosions in $5.0 \cdot 10^7$ yr.

By using the previously defined units, formula (10) concerning “the expansion law” in the bursting phase becomes

$$R = 111.56 \text{ pc} \left(\frac{E_{51} t_7^3 N^*}{n_0} \right)^{\frac{1}{5}}. \quad (25)$$

Conversely, Equation (14) concerning “the expansion law” in the adiabatic phase is

$$R = 171.85 \text{ pc} \left(\frac{E_{51} N^*}{n_0} \right)^{\frac{1}{5}} (t_7^{\text{burst}})^{\frac{11}{35}} (t_7)^{\frac{2}{7}}. \quad (26)$$

This is the approximate radius derived from a spherical model. A perfect coincidence is not expected upon making a comparison with that expected in a stratified medium obtained with the multidimensional thin shell approximation. Another useful formula is the luminosity of the bubble, see [11],

$$L_{\text{SN}} = E_0 R_{\text{SN}} = 0.645^{36} \text{ erg s}^{-1} E_{51} N^*. \quad (27)$$

This formula can be useful in order to derive the parameter N^* from observations; for example, a luminosity of $1.6 \cdot 10^{38} \text{ erg s}^{-1}$ corresponds to $N^* = 248$. The total deposited energy, E_{tot} , is

$$E_{\text{tot}} = E_{51} N^* 10^{51} \frac{t_{\text{age}}}{5 \cdot 10^7 \text{ yr}} \text{ erg}, \quad (28)$$

when $t^{\text{burst}} = t_{\text{age}}$ and

$$E_{\text{tot}} = E_{51} N^* 10^{51} \frac{t^{\text{burst}}}{5 \cdot 10^7 \text{ yr}} \text{ erg}, \quad (29)$$

when $t^{\text{burst}} < t_{\text{age}}$.

The spectrum of the radiation emitted depends on the temperature behind the shock front, see for example formula 9.14 in [36],

$$T = \frac{3}{16} \frac{\mu}{k} v_s^2 \text{ K}^\circ, \quad (30)$$

where μ is the mean mass per particle, k the Boltzmann constant and v_s the shock velocity expressed in cm sec^{-1} . A formula which is useful for the implementation in the code is easily derived,

$$T = 31.80 v_{\text{sk}}^2 \text{ K}^\circ, \quad (31)$$

when v_{sk} is expressed in km sec^{-1} .

4. The Cold model for SBs

This Section reviews the standard thin layer approximation and then introduces two recursive equations for the dynamical evolution of a SB in an auto-gravitating medium, see [37].

4.1. The symmetrical thin layer approximation

The thin layer approximation assumes that all the swept-up gas accumulates infinitely in a thin shell just after the shock front. The conservation of radial momentum requires that

$$\frac{4}{3}\pi R^3 \rho \dot{R} = M_0, \quad (32)$$

where R and \dot{R} are the radius and the velocity of the advancing shock, ρ is the density of the ambient medium, M_0 is the momentum evaluated at $t = t_0$, R_0 is the initial radius, and \dot{R}_0 the initial velocity, see [38, 39]. The law of motion is

$$R = R_0 \left(1 + 4 \frac{\dot{R}_0}{R_0} (t - t_0) \right)^{\frac{1}{4}}, \quad (33)$$

and the velocity

$$\dot{R} = \dot{R}_0 \left(1 + 4 \frac{\dot{R}_0}{R_0} (t - t_0) \right)^{-\frac{3}{4}}. \quad (34)$$

4.2. Asymmetrical law of motion

Given the Cartesian coordinate system (x, y, z) , the plane $z = 0$ will be called the equatorial plane, $z = R \sin(\theta)$, where θ is the latitude angle which has range $[-90^\circ \leftrightarrow +90^\circ]$, and R is the distance from the origin. The latitude angle is often used in astrophysics to model asymmetries in the polar lobes, see the example of the nebula around η -Carinae (Homunculus) shown in Table 1 in [40]. In our framework, the polar angle of the spherical coordinate system is $90 - \theta$. The vertical number density distribution of galactic HI is usually modeled by the three component function as given by eqn. (24). Here, conversely, we adopt the density profile of a thin self-gravitating disk of gas which is characterized by a Maxwellian distribution in velocity and distribution which varies only in the z -direction (ISD). The number density distribution is

$$n(z) = n_0 \text{sech}^2\left(\frac{z}{2h}\right), \quad (35)$$

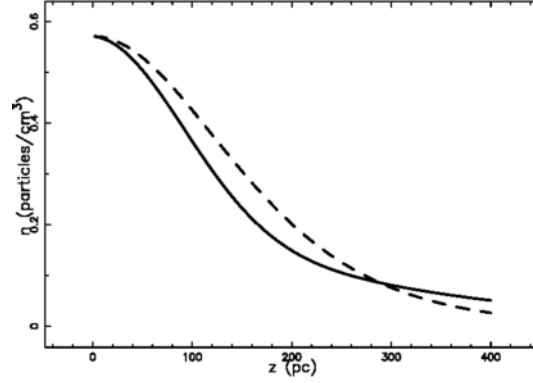


Figure 4. Profiles of density versus scale height z : the self-gravitating disk as given by Eq. (35) when $h = 90$ pc (dashed) and the three-component exponential distribution as given by Eq. (24) (full line).

where n_0 is the density at $z = 0$, h is a scaling parameter, and $sech$ is the hyperbolic secant ([41, 42, 43, 44]).

Figure (4) compares the empirical function sum of three exponential disks and the theoretical function as given by Eq. (35). Assuming that the expansion starts at $z = 0$, we can write $z = R \sin(\theta)$, and therefore

$$n(R, \theta) = n_0 sech^2\left(\frac{R \sin(\theta)}{2h}\right) , \quad (36)$$

where R is the radius of the advancing shell.

The 3D expansion that starts at the origin of the coordinates will be characterized by the following properties.

- The dependence of the momentary radius of the shell on the latitude angle θ over the range $[-90^\circ \leftrightarrow +90^\circ]$.
- The independence of the momentary radius of the shell from ϕ , the azimuthal angle in the x - y plane, which has a range $[0^\circ \leftrightarrow 360^\circ]$.

The mass swept, M , along the solid angle $\Delta \Omega$ between 0 and R is

$$M(R, \theta) = \frac{\Delta \Omega}{3} m_H n_0 I_m(R) + \frac{4}{3} \pi R_0^3 n_0 m_H , \quad (37)$$

where

$$I_m(R) = \int_{R_0}^R r^2 sech^2\left(\frac{r \sin(\theta)}{2h}\right) dr , \quad (38)$$

where R_0 is the initial radius and m_H the mass of hydrogen. The integral is

$$I_m(R) = -4 h r^2 (\sin(\theta))^{-1} \left(1 + e^{\frac{r \sin(\theta)}{h}}\right)^{-1} + 4 \frac{h r^2}{\sin(\theta)} - 8 h^2 r \ln\left(1 + e^{\frac{r \sin(\theta)}{h}}\right) (\sin(\theta))^{-2} - 8 h^3 \text{Li}_2\left(-e^{\frac{r \sin(\theta)}{h}}\right) (\sin(\theta))^{-3} , \quad (39)$$

where

$$\text{Li}_2(z) = \sum_{n=1}^{\infty} \frac{z^n}{n^2} \quad , \quad (40)$$

is the dilogarithm, see [45, 46, 47].

The conservation of momentum along the solid angle $\Delta \Omega$ gives

$$M(R, \theta) \dot{R}(\theta) = M(R_0) \dot{R}_0 \quad , \quad (41)$$

where $\dot{R}(\theta)$ is the velocity at R and \dot{R}_0 is the initial velocity at $R = R_0$. Using the previous equation, an analytical expression for $\dot{R}(\theta)$ along the solid angle can be found, but it is complicated, and therefore we omit it. In this differential equation of the first order in R , the variables can be separated and integrating term by term gives

$$\int_{R_0}^R M(r, \theta) dr = M(R_0) \dot{R}_0 (t - t_0) \quad , \quad (42)$$

where t is the time and t_0 the time at R_0 . We therefore have an equation of the type

$$\mathcal{F}(R, R_0, h)_{NL} = \frac{1}{3} R_0^3 \dot{R}_0 (t - t_0) \quad , \quad (43)$$

where $\mathcal{F}(R, R_0, h)_{NL}$ has an analytical but complicated form. The case of expansion that starts from a given galactic height z , denoted by z_{OB} , which represent the OB associations, cannot be solved by Eq. (43), which is derived for a symmetrical expansion that starts at $z = 0$. It is not possible to find R analytically and a numerical method should be implemented. In our case, in order to find the root of the nonlinear Eq. (43), the FORTRAN subroutine ZRDDR from [32] has been used.

The following two recursive equations are found when momentum conservation is applied:

$$\begin{aligned} R_{n+1} &= R_n + V_n \Delta t \\ V_{n+1} &= V_n \left(\frac{M_n(r_n)}{M_{n+1}(R_{n+1})} \right) \quad , \end{aligned} \quad (44)$$

where R_n , V_n , M_n are the temporary radius, the velocity, and the total mass, respectively, Δt is the time step, and n is the index. The advancing expansion is computed in a 3D Cartesian coordinate system (x, y, z) with the center of the explosion at $(0,0,0)$. The explosion is better visualized in a 3D Cartesian coordinate system (X, Y, Z) in which the galactic plane is given by $Z = 0$. The following translation, T_{OB} , relates the two Cartesian coordinate systems.

$$T_{\text{OB}} \begin{cases} X = x \\ Y = y \\ Z = z + z_{\text{OB}} \end{cases} \quad , \quad (45)$$

where z_{OB} is the distance in parsecs of the OB associations from the galactic plane.

The physical units have not yet been specified: parsecs for length and 10^7 yr for time, see also subsection 3.6., are an acceptable astrophysical choice. With these units, the initial

velocity $V_0 = \dot{R}_0$ is expressed in units of pc/(10^7 yr) and should be converted into km/s; this means that $V_0 = 10.207V_1$ where V_1 is the initial velocity expressed in km/s.

Analytical results can also be obtained solving the Kompaneets equation, see [48], for the motion of a shock wave in different plane-parallel stratified media such as exponential, power-law type, and a quadratic hyperbolic-secant, see synoptic Table 4 in [49].

5. A Comparison with Hydrosimulations

This Section reports the comparison of the thermal and cold models with numerical hydro-dynamics calculations.

5.1. The thermal test

The shape of the SB in the thermal model, see Section 3., depends strongly on the time elapsed since the first explosion, t_{age} , the duration of SN burst, t^{burst} , on the number of SN explosions in the bursting phase, and on the adopted density profile. Ordinarily, the dynamics of an SB is studied with hydro simulations (partial differential equations). Conversely, here under the hypothesis called “thin-shell approximation”, the dynamics is studied by solving ordinary differential equations. This choice allows the calculation of a much larger number of models compared with hydro-dynamics calculations.

The level of confidence in our results can be given by a comparison with numerical hydro-dynamics calculations see, for example, [19]. The vertical density distribution they adopted [see equation(1) from [19] and equation(5) from [50]] has the following z dependence, the distance from the galactic plane in pc:

$$n_{\text{hydro}} = n_d \left\{ \Theta \exp\left[-\frac{V(z)}{\sigma_{IC}^2}\right] + (1 - \Theta) \exp\left[-\frac{V(z)}{\sigma_C^2}\right] \right\}, \quad (46)$$

with the gravitational potential as

$$V(z) = 68.6 \ln \left[1 + 0.9565 \sinh^2 \left(0.758 \frac{z}{z_0} \right) \right] (\text{kms}^{-1})^2. \quad (47)$$

Here $n_d = 1$ particles cm^{-3} , $\Theta = 0.22$, $\sigma_{IC} = 14.4 \text{ km s}^{-1}$, $\sigma_C = 7.1 \text{ km s}^{-1}$ and $z_0 = 124$ pc. Table 2 reports the results of ZEUS (see [19]), a two-dimensional hydro-dynamic code, when $t_{\text{age}} = 0.45 \cdot 10^7$ yr. The supernova luminosity is $1.6 \cdot 10^{38} \text{ erg s}^{-1}$, $z_{\text{OB}}=100$ pc and the density distribution is given by formula (46). The ZEUS code was originally described by [51].

In order to make a comparison our code was run with the parameters of the hydro-code (see Figure 5); a density profile as given by formula (46) was adopted. The percentage of reliability of our code can also be introduced,

$$\epsilon = \left(1 - \frac{|(R_{\text{hydro}} - R_{\text{num}})|}{R_{\text{hydro}}} \right) \cdot 100, \quad (48)$$

where R_{hydro} is the radius, as given by the hydro-dynamics, and R_{num} the radius obtained from our simulation. In the already cited table 2, our numerical radii can also be found in the

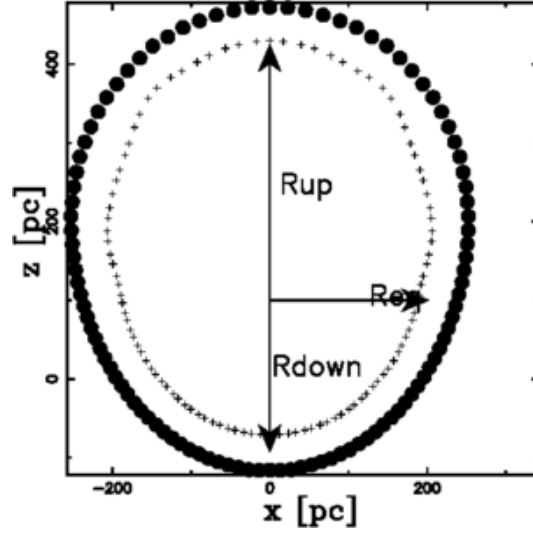


Figure 5. Section of the on the x - z plane when the explosion starts at $z_{\text{OB}} = 100\text{pc}$. The density law is given by Equation 46. The code parameters are $t_{\text{age}}=0.45 \cdot 10^7 \text{ yr}$, $\Delta t = 0.001 \cdot 10^7 \text{ yr}$, $t_7^{\text{burst}}=0.45$, and $N^*=248$. The points represented by the small crosses indicate the inner section from Figure 3a of [19].

Table 2. Code reliability.

	$R_{\text{up}}(\text{pc})$	$R_{\text{down}}(\text{pc})$	$R_{\text{eq}}(\text{pc})$
$R_{\text{hydro}}(\text{ZEUS})$	330	176	198
$R_{\text{num}}(\text{our code})$	395	207	237
efficiency(%)	80	81	80

upward, downward and equatorial directions, and the efficiency as given by formula (48). The value of the radii are comparable in all of the three chosen directions and Figure 5 also reports on the data from Figure 3a of [19].

5.2. The cold test

In the framework of the cold model developed in Section 4. Figure 6 compares the hydro number density as given by Eq. 46 and the theoretical function as given by Eq. (35). The difference in the density profiles from hydrosimulations and from the cold model adopted are due to the fact that the density at $z = 0$ is assumed to be $n_{\text{hydro}} = 1 \text{ particles cm}^{-3}$ in the hydrosimulations, see [19]. In our cold model conversely at $z = 0$ we have $n = 0.566 \text{ particles cm}^{-3}$ as in [35].

A typical run of ZEUS (see [19]), a two-dimensional hydrodynamic code, is done for $t_7 = 0.45$ and supernova luminosity of $1.6 \cdot 10^{38} \text{ erg s}^{-1}$ when $z_{\text{OB}}=100 \text{ pc}$. In order to make

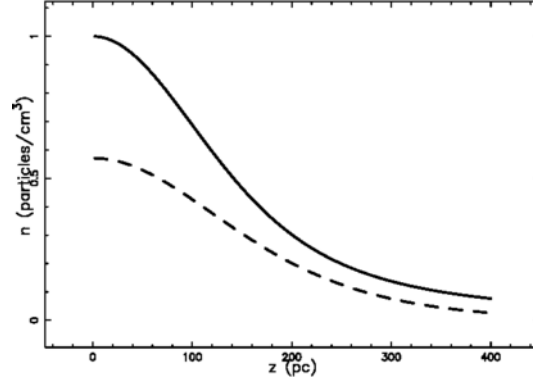


Figure 6. Profiles of density versus scale height z : the self-gravitating disk as in Eq. (35) when $h = 90$ pc (dashed line) and the hydro number density as given by Eq. 46 (full line).

a comparison with our cold code, we adopt the same time and we search the parameters which produce similar results, see Figure 7.

6. Astrophysical SBs

This section evaluates the significance of the galactic rotation for the shape of the SBs, models the thermal GW 46.4+5.5, the thermal Gould Belt, the cold GW 46.4+5.5 and the thermal Galactic Plane.

6.1. Galactic rotation

The influence of the Galactic rotation on the results can be obtained by introducing the law of the Galactic rotation as given by [52],

$$V_R(R_0) = 220 \left(\frac{R_0[\text{pc}]}{8500} \right)^{0.382} \text{km sec}^{-1}, \quad (49)$$

where R_0 is the radial distance from the center of the Galaxy expressed in pc. The translation of the previous formula to the astrophysical units adopted gives

$$V_R(R_0) = 2244 \left(\frac{R_0[\text{pc}]}{8500} \right)^{0.382} \frac{\text{pc}}{10^7 \text{ yr}}, \quad (50)$$

$$\Omega(R_0) = 2244 \frac{\left(\frac{R_0[\text{pc}]}{8500} \right)^{0.382}}{R_0[\text{pc}]} \frac{\text{rad}}{10^7 \text{ yr}}. \quad (51)$$

Here, $\Omega(R_0)$ is the differential angular velocity and

$$\phi = 2244 \frac{\left(\frac{R_0[\text{pc}]}{8500} \right)^{0.382}}{R_0[\text{pc}]} t_7 \text{ rad}. \quad (52)$$

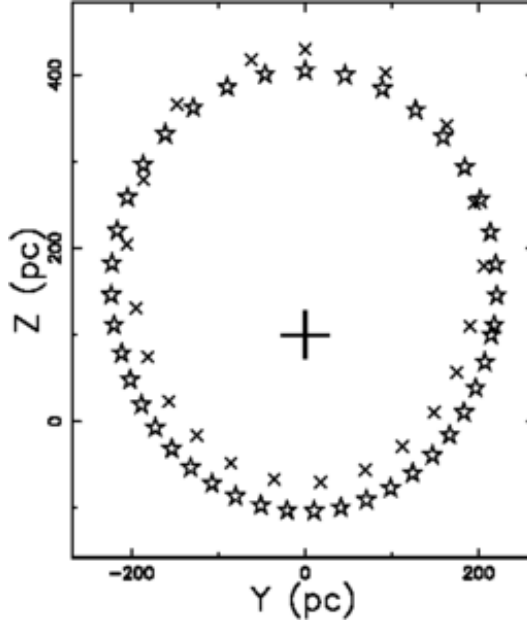


Figure 7. Section of the SB in the X - Z plane when the explosion starts at $z_{OB} = 100\text{pc}$ (empty stars). The cold code parameters are $h = 90\text{ pc}$, $t_7 = 0.45$, $t_{7,0} = 0.00045$, $r_0 = 24.43$, $V_0 = 3191\text{ km s}^{-1}$, $N_{SN} = 180$ and $N^* = 2000000$. The points represented by the small crosses indicate the inner section from Figure 3a of MacLow et al. 1989. The explosion site is represented by a big cross.

Here, ϕ , is the angle made on the circle and t_7 the time expressed in units of 10^7 yr. Upon considering only a single object, an expression for the angle can be found once $R = R_0 + y$ is introduced,

$$\phi(y) = \frac{V_R(R_0)}{R_0 + y} t. \quad (53)$$

The shift in the angle due to differential rotation can now be introduced,

$$\Delta\phi = \phi(y) - \phi(0), \quad (54)$$

where x and y are the SB coordinates in the inertial frame of the explosion, denoted by $x=0, y=0$ and $z=z_{OB}$. The great distance from the center allows us to say that

$$\frac{\Delta x}{R_0} = \Delta\phi, \quad (55)$$

where Δx is the shift due to the differential rotation in the x coordinate. The shift can be found from (55) and (54) once a Taylor expansion is performed,

$$\Delta x \approx -V_R(R_0) \frac{y}{R_0} t. \quad (56)$$

Upon inserting (50) in (56), the following transformation, T_r , due to the rotation is obtained for a single object in the solar surroundings:

$$T_r \begin{cases} x' = x + 0.264y t \\ y' = y \\ z' = z, \end{cases} \quad (57)$$

where y is expressed in pc and t in units of 10^7 yr.

6.2. Thermal GW 46.4+5.5

A careful study of the worms 46.4+5.5 and 39.7+5.7 [53] has led to the conclusion that they belong to a single super-shell. Further on, the dynamical properties of this HI supershell can be deduced by coupling the observations with theoretical arguments, [54]; the derived model parameters to fit the observations are reported in Table 3, where the altitudes of KK 99 3 and KK 99 4 (clouds that are CO emitters) have been identified with z_{OB} by the author.

These parameters are the input for our thermal computer code (see the captions of Figure 8). The problem of assigning a value to z_{OB} now arises, and the following two equations are set up:

$$\begin{aligned} R_{up} + z_{OB} &= 540, \\ \frac{R_{up} + z_{OB}}{R_{down} - z_{OB}} &= \frac{D_{up}}{D_{down}} = \frac{15^\circ}{3^\circ} = 3. \end{aligned} \quad (58)$$

The algebraic system (58) consists of two equations and three variables. The value chosen for the minimum and maximum latitudes (15° and -5°) are in rough agreement with the

Table 3. Data of the supershell associated with GW 46.4+5.5.

Size (pc ²)	345 · 540
Expansion velocity (km s ⁻¹)	15
Age (10 ⁷ yr)	0.5
z_{OB} (pc)	100
Total energy (10 ⁵¹ erg)	15

Table 4. Radii concerning GW 46.4+5.5.

Direction	R_{num} (pc)	R_{num} (pc) with the Euler process	R_{obs} (pc)
Equatorial	238	233	172.5
Polar up	342	335	305
Polar down	312	304	235

position of the center at $+5^\circ$ of the galactic latitude (see [55]). One way of solving 58 is to set, for example, $z_{OB}=100$ pc. The other two variables are easily found to be as follows:

$$\begin{aligned}
 z_{OB} &= 100 \text{ pc}, \\
 R_{\text{down}} &= 235 \text{ pc}, \\
 R_{\text{up}} &= 305 \text{ pc}.
 \end{aligned} \tag{59}$$

For this value of z_{OB} , we have the case where a transition from an egg-shape to a V-shape is going on, and the simulation gives the exact shape. In order to obtain $E_{\text{tot}} = 15 \cdot 10^{51} \text{ erg}$ (see formula (29)) and $t^{\text{burst}} = 0.5 \cdot 10^7 \text{ yr}$, we have inserted $N^* = 150$.

In order to test our simulation, an observational percentage of reliability is introduced that uses both the size and the shape,

$$\epsilon_{\text{obs}} = 100 \left(1 - \frac{\sum_j |R_{\text{obs}} - R_{\text{num}}|_j}{\sum_j R_{\text{obs}j}} \right), \tag{60}$$

where R_{obs} is the observed radius, as deduced by using the following algorithm. The radius at regular angles from the vertical (0° , 90° , 180°) is extracted from Table 3, giving the series (305 pc, 172.5 pc, 235 pc); the theory of cubic splines [32] is then applied to compute the various radii at progressive angles (0° , 3.6° , 7.2° , ..., 180°), which is a series computed by adding regular steps of $180^\circ/n_\theta$. The data are extracted from the dotted ellipse visible in Figure 7 of [55]; this ellipse represents the super-shell at $v_{LSR} = 18.5 \text{ km sec}^{-1}$.

We can now compute the efficiency over 50+1 directions [formula (60)] of a section y-z when $x=0$ which turns out to be $\epsilon_{\text{obs}} = 68.4\%$; the observed and numerical radii along the three typical directions are reported in Table 4. The physical parameters adopted from [53] turn out to be consistent with our thermal numerical code. The results of the simulation can be visualized in Figure 8, or through a section on the x - z plane (see Figure 9). Another

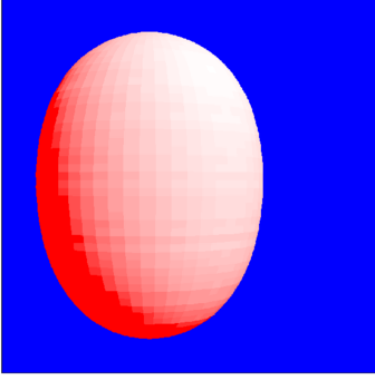


Figure 8. Model of GW 46.4+5.5. The parameters are $t_{\text{age}}=0.5 \cdot 10^7$ yr, $\Delta t = 0.001 \cdot 10^7$ yr, $t_7^{\text{burst}} = 0.5$, $N^* = 150$, $z_{\text{OB}}=100$ pc, and $E_{51}=1$. The three Eulerian angles characterizing the point of view of the observer are $\Phi=0^\circ$, $\Theta=90^\circ$ and $\Psi=0^\circ$.

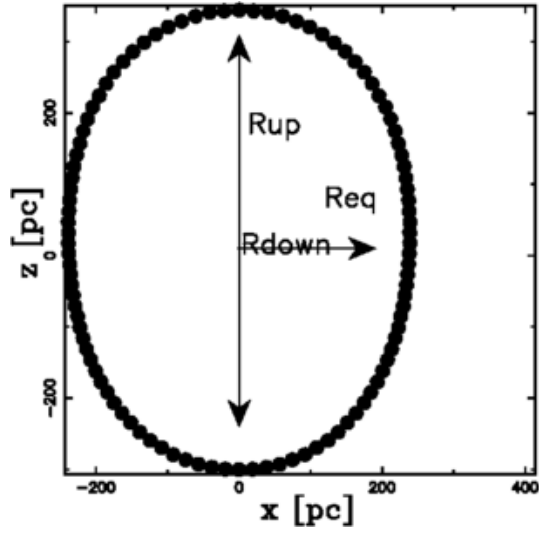


Figure 9. Section of the SB on the x - z plane when the physical parameters are the same as in Figure 8.

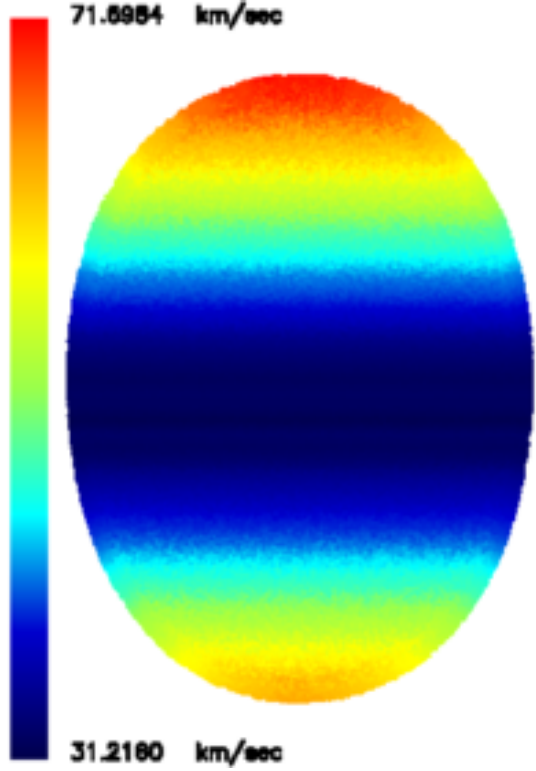


Figure 10. Map of the expansion velocity relative to a simulation of GW 46.4+5.5 when 190000 random points are selected on the surface. The physical parameters are the same as in Figure 8 and the three Eulerian angles characterizing the point of view of the observer are $\Phi = 0^\circ$, $\Theta = 90^\circ$, and $\Psi = 0^\circ$.

important observational parameter is the HI 21 cm line emission: the observation of HI gas associated with GW 46.4+5 [56, 53] reveals that the super-shell has an expansion velocity of $V_{\text{exp}} \approx 15 \text{ km s}^{-1}$ [53]. In order to see how our model matches the observations, the instantaneous radial velocities are computed in each direction. A certain number of random points are then generated on the theoretical surface of expansion. The relative velocity of each point is computed by using the method of bilinear interpolation on the four grid points that surround the selected latitude and longitude [32].

Our model gives radial velocities of V_{theo} , $31 \text{ km s}^{-1} \leq V_{\text{theo}} \leq 71 \text{ km s}^{-1}$ ($27 \text{ km s}^{-1} \leq V_{\text{theo}} \leq 66 \text{ km s}^{-1}$ with the Euler process) and a map of the expansion velocity is given in Figure 10, from which it is possible to visualize the differences in the expansion velocities between the various regions.

Perhaps it is useful to map the velocity ($V_{\text{theo}}^{\text{p}}$) in the y-direction,

$$V_{\text{theo}}^{\text{p}} = v(\theta, \phi) \cdot \sin(\theta) \cdot (\sin \phi). \quad (61)$$

This is the velocity measured along the line of sight when an observer stands in front of the super-bubble; θ and ϕ were defined in subsection 3.2.. The structure of the projected velocity, $V_{\text{theo}}^{\text{p}}$, is mapped in Figure 11 by using different colors; the range is 0 km s^{-1}

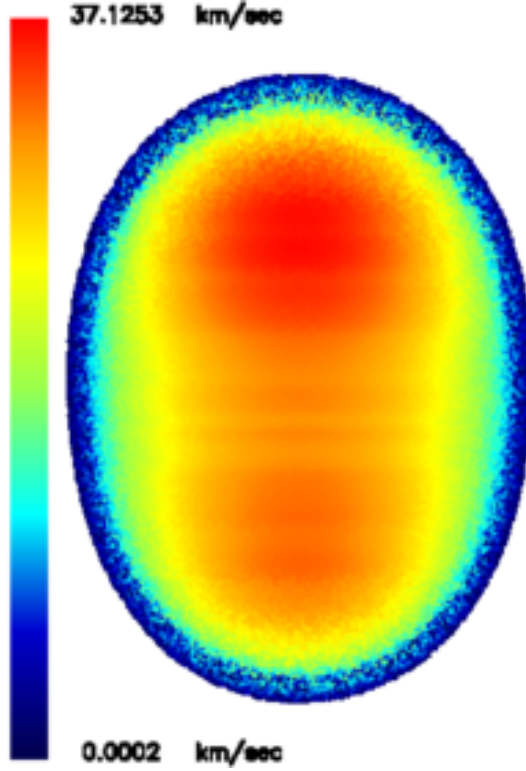


Figure 11. Map of the velocity along the line of sight, V_{theo}^p , relative to a simulation of GW 46.4+5.5 when 190000 random points are selected on the surface. The physical parameters are the same as in Figure 11.

$\leq V_{\text{theo}}^p \leq 36 \text{ km s}^{-1}$ ($0 \text{ km s}^{-1} \leq V_{\text{theo}}^p \leq 32 \text{ km s}^{-1}$ with the Euler process) and the averaged projected velocity is $\approx 20 \text{ km s}^{-1}$ ($\approx 17.6 \text{ km s}^{-1}$ with the Euler process), a value that is greater by $\approx 5 \text{ km s}^{-1}$ ($\approx 2.6 \text{ km s}^{-1}$ with the Euler process) than the already mentioned observed expansion velocity, $V_{\text{exp}} = 15 \text{ km s}^{-1}$.

As is evident from the map in Figure 11, the projected velocity of expansion is not uniform over all of the shell's surface, but is greater in the central region than in the external region. In this particular case of an egg-shape, we observe a nearly circular region connected with the maximum velocities in the upper part of the shell. It is therefore possible to speak of egg-shaped appearances in the Cartesian physical coordinates and spherical appearances in the projected maximum velocity.

6.3. Thermal Gould Belt

The physical parameters concerning the Gould Belt as deduced in [57], are reported in Table 5. The total energy is such as to produce results comparable with the observations and the kinematic age is the same as in [57, 58]. In order to obtain $E_{\text{tot}} = 6 \cdot 10^{51} \text{ erg}$ with $t^{\text{burst}} = 0.015 \cdot 10^7 \text{ yr}$, we have inserted $N^* = 2000$. The time necessary to cross the Earth's orbit, that lies 104 pc away from the Belt center, turns out to be $0.078 \cdot 10^7 \text{ yr}$, which means $2.52 \cdot 10^7 \text{ yr}$ from now. The 2D cut at $z=0$ of the SB can be visualized in Figure 12. Our

Table 5. Data of the super-shell associated with the Gould Belt

Size (pc^2)	$466 \cdot 746$ at $b=0$
Expansion velocity (km s^{-1})	17
Age (10^7 yr)	2.6
Total energy (10^{51} erg)	6

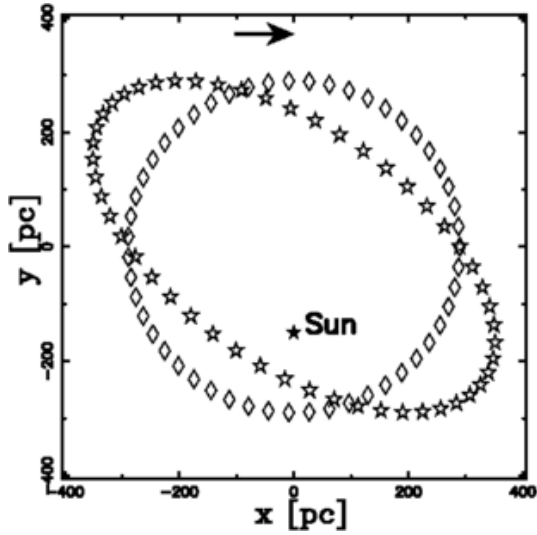


Figure 12. Rhombi represent the circular section, the stars the rotation-distorted section and the big star the Sun. The Galaxy's direction of rotation is also shown. The parameters are $t_{\text{age}}=2.6 \cdot 10^7 \text{ yr}$, $\Delta t = 0.001 \cdot 10^7 \text{ yr}$, $t_7^{\text{burst}}=0.015$, $N^*=2000$, $z_{\text{OB}}=0 \text{ pc}$, and $E_{51}=1$.

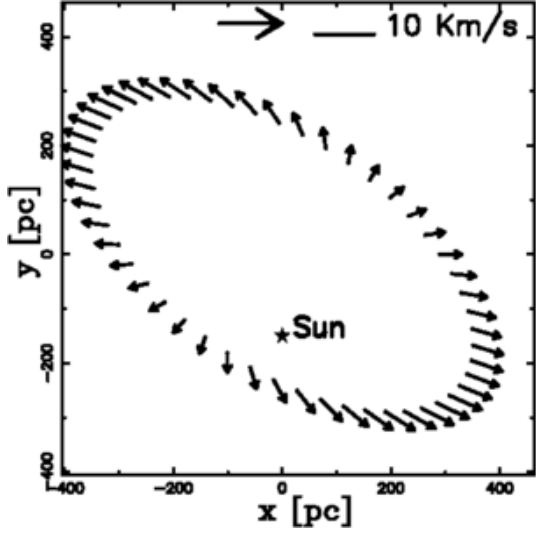


Figure 13. The stars represent the rotation-distorted section of the Gould Belt and the big star the Sun. The velocity field of the expansion modified by the shear velocity is mapped. The Galaxy's direction of rotation is also shown.

Table 6. Simulated data of the SB associated with GW 46.4+5.5.

Size (pc^2)	454 · 521
Averaged expansion velocity (km s^{-1})	19.3
Age (10^7 yr)	0.45
z_{OB} (pc)	100

thermal model gives a radial velocity at $z=0$ of $V_{\text{theo}}=3.67 \text{ km s}^{-1}$. The influence of the Galactic rotation on the direction and modulus of the field of the radial velocity is obtained by an application of transformation (50), see Figure 13. A comparison should be made with figure 5 and figure 9 in [57].

6.4. Cold GW 46.4+5.5

The analytical cold model as given by the solution of the nonlinear Eq. (43) can be used only in the case $z_{OB}=0$. As an example, we give a model of the SB associated with GW 46.4+5.5, see Figure 14. The numerical solution as given by the recursive relation (44) can be found adopting the same input data as the analytical solution, see the crosses in Figure (14); the numerical solution agrees with the analytical solution within 0.65%. We are now ready to present the numerical evolution of the SB associated with GW 46.4+5 when $z_{OB} = 100\text{pc}$, see Figure 15 and Table 6.

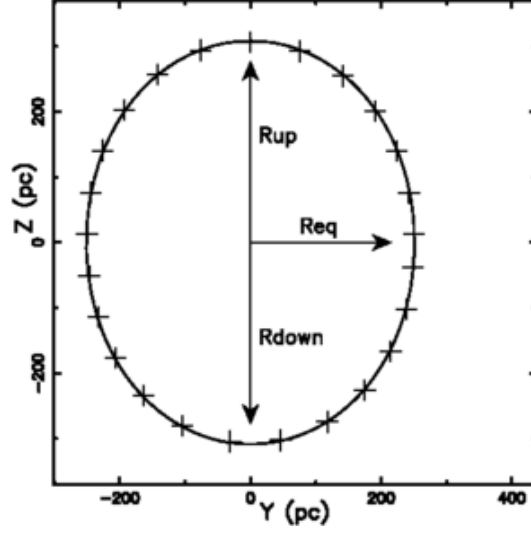


Figure 14. Section of the SB GW 46.4+5 in the Y - Z ; $X=0$ plane when the explosion starts at $z_{OB} = 0$ pc. The analytical results are shown as a full line and the numerical results as crosses. The cold code parameters of the solution of Eq. (43) as well of the numerical couple (44) are $h = 90$ pc, $t_7 = 0.45$, $t_{7,0} = 0.0045$, $r_0 = 49.12$, $V_0 = 641.7 \text{ km s}^{-1}$, $N_{SN} = 93$ and $N^* = 103000$.

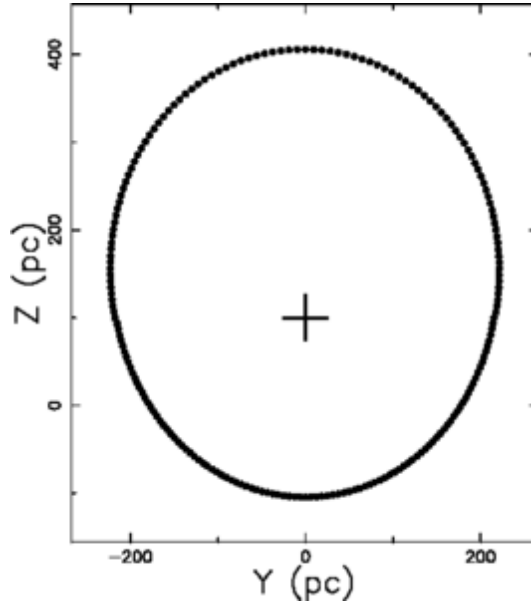


Figure 15. Section of the SB GW 46.4+5 in the Y - Z ; $X=0$ plane when the explosion starts at $z_{OB} = 100$ pc. The cold code parameters for the numerical couple (44) are $h = 90$ pc, $t_7 = 0.45$, $t_{7,0} = 0.00045$, $r_0 = 24.43$, $V_0 = 3191 \text{ km s}^{-1}$, $N_{SN} = 180$ and $N^* = 2000000$. The explosion site is represented by a cross.

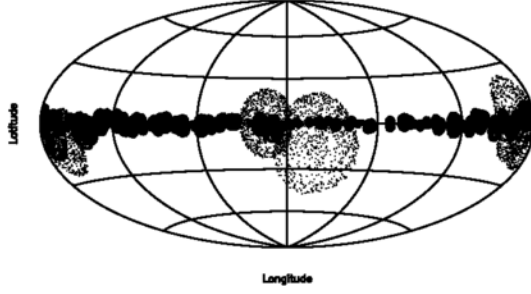


Figure 16. Structure of the galactic plane in the Hammer–Aitoff projection, as resulting from the SB/percolation network. The value of p_{select} is 0.08, corresponding to 260 selected clusters. The parameters were $\Delta t = 0.01 \cdot 10^7$ yr, $t_7^{\text{burst}} = 0.5$, $N^* = 100$ and each SB had 200 random points on its surface.

6.5. The thermal Galactic Plane

In order to simulate the structure of the galactic plane, the same basic parameters as in Figure 1 can be chosen, but now the SBs are drawn on an equal-area Aitoff projection. In particular, a certain number of clusters will be selected through a random process according to the following formula:

$$\text{selected clusters} = p_{\text{select}} \cdot \text{number of clusters from percolation}, \quad (62)$$

where p_{select} has a probability lower than one. The final result of the simulation for the thermal case is reported in Figure 16.

7. Theory of the Image

The transfer equation in the presence of emission only, see for example [59] or [60], is

$$\frac{dI_\nu}{ds} = -k_\nu \zeta I_\nu + j_\nu \zeta, \quad (63)$$

where I_ν is the specific intensity, s is the line of sight, j_ν the emission coefficient, k_ν a mass absorption coefficient, ζ the mass density at position s , and the index ν denotes the relevant frequency of emission. The solution to Eq. (63) is

$$I_\nu(\tau_\nu) = \frac{j_\nu}{k_\nu} (1 - e^{-\tau_\nu(s)}) , \quad (64)$$

where τ_ν is the optical depth at frequency ν

$$d\tau_\nu = k_\nu \zeta ds . \quad (65)$$

We now continue analysing the case of an optically thin layer in which τ_ν is very small (or k_ν very small) and the density ζ is replaced with our number density $C(s)$ of particles. One case is taken into account: the emissivity is proportional to the number density

$$j_\nu \zeta = KC(s) , \quad (66)$$

where K is a constant. This can be the case for synchrotron emission. We select as an example the [S II] continuum of the synchrotron SB in the irregular galaxy IC10, see [61], and the X-ray emission below 2 keV around the OB association LH9 in the H II complex N11 in the Large Magellanic Cloud, see [62]. The intensity at a given frequency is

$$I(\nu) \propto l\nu^\beta, \quad (67)$$

where l is the length of the radiating region along the line of sight. The synchrotron luminosity is assumed to be proportional to the flow of kinetic energy L_m ,

$$L_m = \frac{1}{2}\rho AV^3, \quad (68)$$

where A is the considered area, see formula (A28) in [63]. In our case, $A = 4\pi R^2$, which means

$$L_m = \frac{1}{2}\rho 4\pi R^2 V^3, \quad (69)$$

where R is the instantaneous radius of the SB and ρ is the density in the advancing layer in which the synchrotron emission takes place. The astrophysical version of the rate of kinetic energy is

$$L_{ma} = 1.39 \times 10^{29} n_1 R_1^2 V_1^3 \frac{ergs}{s}, \quad (70)$$

where n_1 is the number density expressed in units of $1 \frac{particle}{cm^3}$, R_1 is the radius in parsecs, and V_1 is the velocity in km/s. The spectral luminosity, L_ν , at a given frequency ν is

$$L_\nu = 4\pi D^2 S_\nu, \quad (71)$$

with

$$S_\nu = S_0 \left(\frac{\nu}{\nu_0}\right)^\beta, \quad (72)$$

where S_0 is the flux observed at the frequency ν_0 and D is the distance. The total observed synchrotron luminosity, L_{tot} , is

$$L_{tot} = \int_{\nu_{min}}^{\nu_{max}} L_\nu d\nu, \quad (73)$$

where ν_{min} and ν_{max} are the minimum and maximum frequencies observed. The total observed luminosity can be expressed as

$$L_{tot} = \epsilon L_{ma}, \quad (74)$$

where ϵ is a constant of conversion from the mechanical luminosity to the total observed luminosity in synchrotron emission.

The fraction of the total luminosity deposited in a band f_c is

$$f_c = \frac{\nu_{c,min}^{\beta+1} - \nu_{c,max}^{\beta+1}}{\nu_{min}^{\beta+1} - \nu_{max}^{\beta+1}}, \quad (75)$$

where $\nu_{c,min}$ and $\nu_{c,max}$ are the minimum and maximum frequencies of the band. Table 7. shows some values of f_c for the most important optical bands. An analytical solution

Table 7. Table of the values of f_c when $\nu_{min} = 10^7 Hz$, $\nu_{max} = 10^{18} Hz$ and $\beta = -0.7$.

band	λ (Å)	FWHM (Å)	f_c
U	3650	700	6.86×10^{-3}
B	4400	1000	7.70×10^{-3}
V	5500	900	5.17×10^{-3}
$H\alpha$	6563	100	0.56×10^{-3}
[SII] continuum	7040	210	0.92×10^{-3}

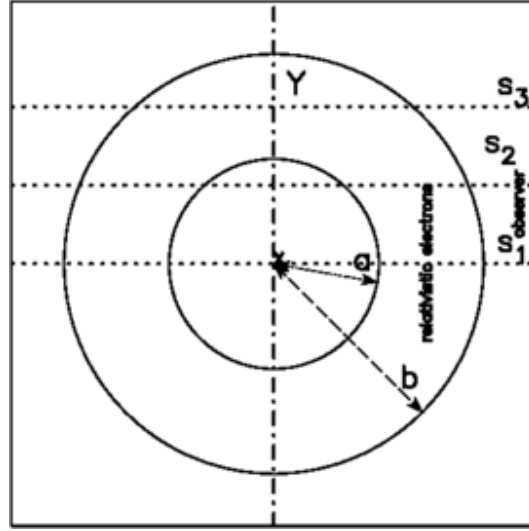


Figure 17. The two circles (sections of spheres) which include the region with constant density are represented by a full line. The observer is situated along the x direction, three lines of sight are indicated, and the relativistic electrons have radius r in the region $a < r < b$.

for the radial cut of intensity of emission can be found in the equatorial plane $z_{OB}=0$. We assume that the number density of relativistic electrons C is constant and in particular rises from 0 at $r = a$ to a maximum value C_m , remains constant up to $r = b$, and then falls again to 0, see [64]. This geometrical description is shown in Figure 17. The length of sight when the observer is situated at the infinity of the x -axis is the locus parallel to the x -axis which crosses the position y in a Cartesian $x - y$ plane and terminates at the external circle of radius b . When the number density of the relativistic electrons C_m is constant between the two spheres of radii a and b , the intensity of the radiation is

$$\begin{aligned}
 I_{0a} &= C_m \times 2 \times (\sqrt{b^2 - y^2} - \sqrt{a^2 - y^2}) \quad ; 0 \leq y < a \\
 I_{ab} &= C_m \times 2 \times (\sqrt{b^2 - y^2}) \quad ; a \leq y < b \quad .
 \end{aligned}
 \tag{76}$$

The ratio between the theoretical intensity at the maximum ($(y = a)$) and at the minimum

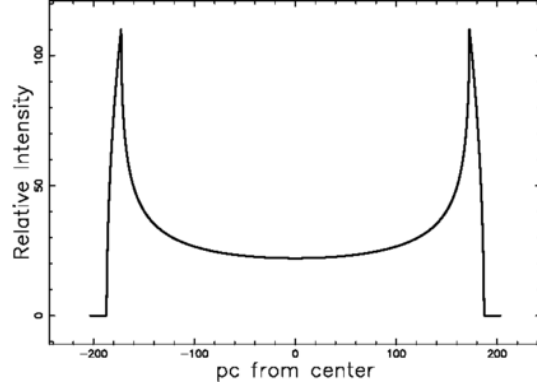


Figure 18. Cut of the mathematical intensity I of the ring model, Eq. (76), in the equatorial plane (full line) of the SB associated with GW 46.4+5.5. The x - and y -axes are in pc, $a = 172.5$ pc, $b = 186.9$ pc and $\frac{I(y=a)}{I(y=0)} = 5$.

($y = 0$) is given by

$$\frac{I(y=a)}{I(y=0)} = \frac{\sqrt{b^2 - a^2}}{b - a} . \quad (77)$$

A cut in the theoretical intensity of the SB associated with GW 46.4+5.5 is shown in Figure 18. Similar analytical results for the intensity of the cuts in the $H\alpha$ region of planetary nebulae and in the radio emission of supernova remnants have been found by [65], compare their figure 5 with our Figure 17, and by [66], see their figure 1. A simulated image of the complex shape of an SB is composed by combining the intensities which characterize different points of the advancing shell. For an optically thin medium, the transfer equation provides the emissivity to be multiplied by the distance of the line of sight, l . This length, in an SB, depends on the orientation of the observer, but for the sake of clarity the observer is at infinity and sees the SB from the equatorial plane $z_{OB} = 0$ or from one of the two poles. We now outline the numerical algorithm which allows us to build the complex image of an SB.

- An empty (value=0) memory grid $\mathcal{M}(i, j, k)$ which contains $NDIM^3$ pixels is initialized.
- We first generate an internal 3D surface by rotating the section of 180° around the polar direction and a second external surface at a fixed distance ΔR from the first surface. As an example, we fixed $\Delta R = 0.03R_{max}$, where R_{max} is the maximum radius of expansion. The points on the memory grid which lie between the internal and the external surfaces are memorized on $\mathcal{M}(i, j, k)$ with a variable integer number according to formula (69) and density ρ proportional to the swept mass.
- Each point of $\mathcal{M}(i, j, k)$ has spatial coordinates x, y, z which can be represented by

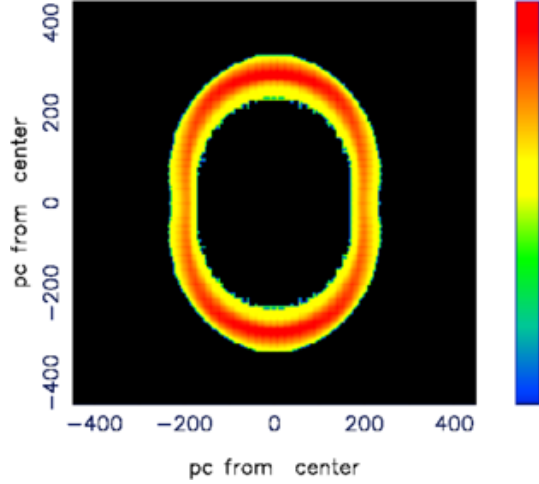


Figure 19. Map of the theoretical intensity of SB GW 46.4+5. Physical parameters as in Figure 14. The three Euler angles characterizing the orientation are $\Phi=90^\circ$, $\Theta=90^\circ$ and $\Psi=90^\circ$. This combination of Euler angles corresponds to the rotated image with the polar axis along the z -axis. In this map $I_{tr} = I_{max}/2$.

the following 1×3 matrix, A ,

$$A = \begin{bmatrix} x \\ y \\ z \end{bmatrix} . \quad (78)$$

The orientation of the object is characterized by the Euler angles (Φ, Θ, Ψ) and therefore by a total 3×3 rotation matrix, E , see [67]. The matrix point is represented by the following 1×3 matrix, B ,

$$B = E \cdot A . \quad (79)$$

- The intensity map is obtained by summing the points of the rotated images along a particular direction.
- The effect of the insertion of a threshold intensity, I_{tr} , given by the observational techniques, is now analyzed. The threshold intensity can be parametrized by I_{max} , the maximum value of intensity which characterizes the map, see [68].

An ideal image of the intensity of SB GW 46.4+5 is shown in Figure 19, and Figure 20 shows two cuts through the center of the SB.

We can also build the theoretical image as seen from one of the two poles, see Figure 21.

We can also visualize the structure of the SBs as seen from an observer situated outside the Galaxy; the spiral structure arising from the ensemble of the shells is evident (see Figure 22). The elliptical shape of the SB, according to formula (52), is a function of both the age and the distance from the center. The distortion follows the inclination of the arms.

Figure 23 reports the image of a galaxy as seen edge on.

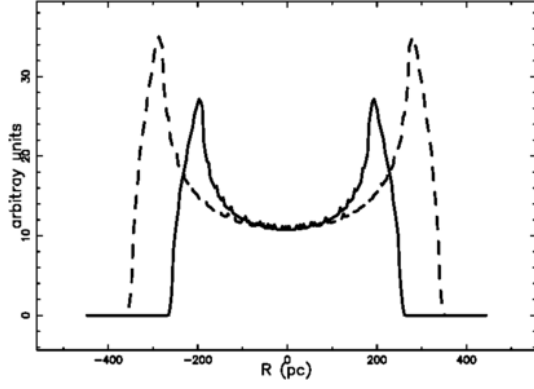


Figure 20. Two cuts of the model intensity across the center of the SB: equatorial cut (full line) and polar cut (dotted line). Parameters as in Figure 19 and $I_{tr} = 0$.

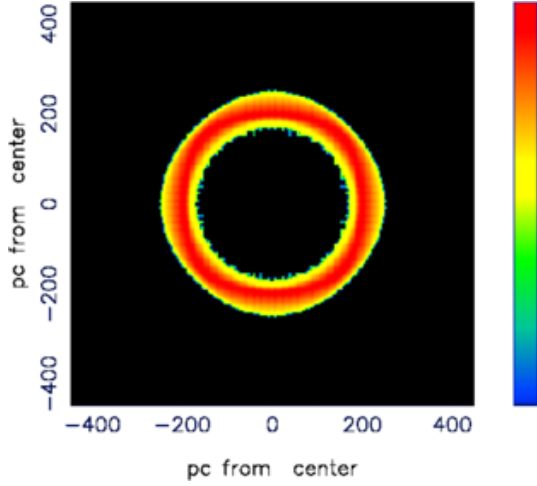


Figure 21. Map of the theoretical intensity of SB GW 46.4+5 as seen from the polar direction at infinity. Physical parameters as in Figure 14. The three Euler angles characterizing the orientation are $\Phi=0^\circ$, $\Theta=0^\circ$ and $\Psi=0^\circ$. In this map $I_{tr} = I_{max}/2$.

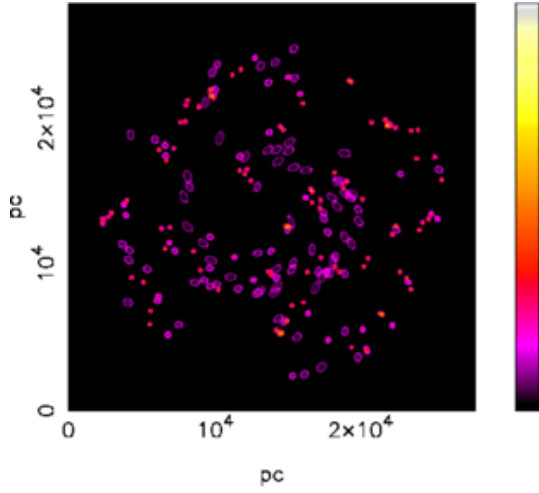


Figure 22. Map of the theoretical intensity of the Milky Way relative to the network of the explosions when the galaxy is face on. Physical parameters as in Figure 16.

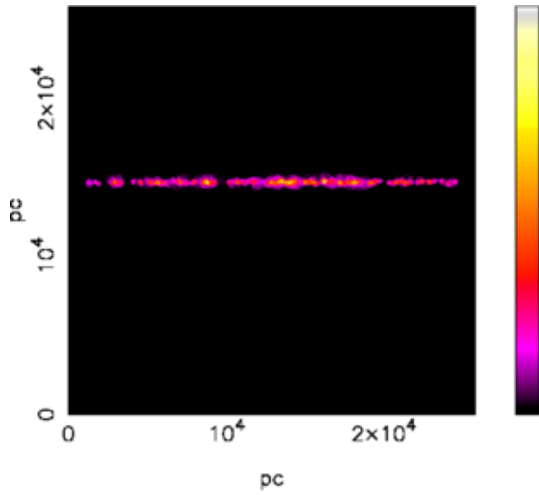


Figure 23. Map of the theoretical intensity of the Milky Way relative to the network of the explosions when the galaxy is edge on. Physical parameters as in Figure 16.

8. Conclusions

Percolation and Spiral Galaxies The active regions of the percolation theory for spirals are usually connected with the SNRs but also the SBs can trigger the formation of new stars.

Thermal law of motion The expansion of a super-bubble in the ISM belonging to our galaxy can be simulated by applying Newton's second law to different pyramidal sectors. The following results were achieved:

1. Single objects, like the super-shells associated with GW 46.4+5 and GSH 238, were simulated with an efficiency of $\epsilon_{\text{obs}} \approx 68\%$ and $\epsilon_{\text{obs}} \approx 58\%$, respectively.
2. The network of many explosions that originate from the galactic plane could be tentatively simulated.

Cold and asymmetrical law of motion The temporal evolution of an SB in a medium with constant density is characterized by a spherical symmetry. The presence of a thin self-gravitating disk of gas which is characterized by a Maxwellian distribution in velocity and a distribution of density which varies only in the z -direction produces an axial symmetry in the temporal evolution of an SB. The resulting Eq. (43) has an analytical form which can be solved numerically when $z_{\text{OB}} = 0$. The case of $z_{\text{OB}} \neq 0$ can be attacked solving two recursive equations, see (44).

Astrophysical Applications

The thermal model was applied to GW 46.4+5.5, with an efficiency of $\epsilon_{\text{obs}} = 68.4\%$, see Section 6.2., and to the Gould Belt, for which a map of the velocities as modified by the galactic rotation is reported, see Figure 13. The cold model was applied to GW 46.4+5.5.

Images

The combination of different processes such as the complex shape of SBs, the thin layer approximation (which means an advancing layer having a thickness $\approx 1/10$ of the momentary radius), the conversion of the rate of kinetic energy into luminosity and the observer's point of view allows simulating the map of the theoretical intensity of GW 46.4+5.5, see Figure 19. The grand design of the SBs in a spiral network is also simulated, see Figure 22.

Acknowledgments

The credit for Figure 2 is given to JPL/Caltech. At the moment of writing some animations concerning the spiral galaxies as modeled by percolation theory are available at <http://personalpages.to.infn.it/~zaninett/animations.html>.

References

- [1] Heiles, C., H I shells and supershells, ApJ 229 (1979) 533.
- [2] Puche, D., Westpfahl, D., Brinks, E., & Roy, J.-R., Holmberg II—A laboratory for studying the violent interstellar medium, AJ 103 (1992) 1841.
- [3] Walter, F., Kerp, J., Duric, N., Brinks, E., & Klein, U., X-Ray Emission from an Expanding Supergiant Shell in IC 2574, ApJ 502 (1998) L143.

-
- [4] Pikel’Ner, S. B., Interaction of Stellar Wind with Diffuse Nebulae, *Astrophys. Lett.* 2 (1968) 97.
 - [5] Weaver, R., McCray, R., Castor, J., Shapiro, P., & Moore, R., Interstellar bubbles. II—Structure and evolution, *ApJ* 218 (1977) 377.
 - [6] Tenorio-Tagle, G. & Bodenheimer, P., Large-scale expanding superstructures in galaxies, *ARA&A* 26 (1988) 145.
 - [7] Santillán, A., Franco, J., Martos, M., & Kim, J., The Collisions of High-Velocity Clouds with a Magnetized Gaseous Galactic Disk, *ApJ* 515 (1999) 657.
 - [8] Koo, B.-C., Heiles, C., & Reach, W. T., Galactic worms. I—Catalog of worm candidates, *ApJ* 390 (1992) 108.
 - [9] Ambrocio-Cruz, P., Le Coarer, E., Rosado, M., et al., The kinematical properties of superbubbles and H II regions of the Large Magellanic Cloud derived from the 3D H α Survey, *MNRAS* 457 (2016) 2048.
 - [10] Sánchez-Cruces, M., Rosado, M., Rodríguez-González, A., & Reyes-Iturbide, J., Kinematics of Superbubbles and Supershells in the Irregular Galaxy, NGC 1569, *ApJ* 799 (2015) 231.
 - [11] McCray, R. A., Coronal interstellar gas and supernova remnants, in: A. Dalgarno & D. Layzer (Ed.), *Spectroscopy of Astrophysical Plasmas*, Cambridge University Press, Cambridge, 1987, pp. 255–278.
 - [12] McCray, R. & Kafatos, M., Supershells and propagating star formation, *ApJ* 317 (1987) 190.
 - [13] Mac Low, M.-M. & McCray, R., Superbubbles in disk galaxies, *ApJ* 324 (1988) 776.
 - [14] Igumenshchev, I. V., Shustov, B. M., & Tutukov, A. V., Dynamics of supershells—Blow-out, *A&A* 234 (1990) 396.
 - [15] Basu, S., Johnstone, D., & Martin, P. G., Dynamical Evolution and Ionization Structure of an Expanding Superbubble: Application to W4, *ApJ* 516 (1999) 843.
 - [16] Bisnovatyi-Kogan, G. S. & Silich, S. A., Shock-wave propagation in the nonuniform interstellar medium, *Reviews of Modern Physics* 67 (1995) 661.
 - [17] Begelman, M. C. & Li, Z.-Y., An axisymmetric magnetohydrodynamic model for the Crab pulsar wind bubble, *ApJ* 397 (1992) 187.
 - [18] Moreno, E., Alfaro, E. J., & Franco, J., The Kinematics of Stars Emerging from Expanding Shells: An Analysis of the Gould Belt, *ApJ* 522 (1999) 276.
 - [19] Mac Low, M.-M., McCray, R., & Norman, M. L., Superbubble blowout dynamics, *ApJ* 337 (1989) 141.

-
- [20] Ferriere, K. M., Mac Low, M.-M., & Zweibel, E. G., Expansion of a superbubble in a uniform magnetic field, *ApJ* 375 (1991) 239.
 - [21] Tomisaka, K., The evolution of a magnetized superbubble, *PASJ* 44 (1992) 177.
 - [22] Tomisaka, K., Superbubbles in magnetized interstellar media: Blowout or confinement?, *MNRAS* 298 (1998) 797.
 - [23] Kamaya, H., Final Size of a Magnetized Superbubble, *ApJ* 493 (1998) L95.
 - [24] Seiden, P. E. & Gerola, H., Properties of spiral galaxies from a stochastic star formation model, *ApJ* 233 (1979) 56.
 - [25] Seiden, P. E., The role of the gas in propagating star formation, *ApJ* 266 (1983) 555.
 - [26] Schulman, L. S. & Seiden, P. E., Percolation and galaxies, *Science* 233 (1986) 425.
 - [27] Zaninetti, L., Percolation and synchrotron emission. I—The case of spiral galaxies, *A&A* 190 (1988) 17.
 - [28] Seiden, P. E. & Schulman, L. S., Percolation model of galactic structure, *Advances in Physics* 39 (1990) 1.
 - [29] Jungwiert, B. & Palous, J., Stochastic self-propagating star formation with anisotropic probability distribution, *A&A* 287 (1994) 55.
 - [30] Palous, J., Tenorio-Tagle, G., & Franco, J., Star formation in differentially rotating galactic disks: The physics of self-propagation, *MNRAS* 270.
 - [31] Zaninetti, L., On the Shape of Superbubbles Evolving in the Galactic Plane, *PASJ* 56 (2004) 1067.
 - [32] Press, W. H., Teukolsky, S. A., Vetterling, W. T., & Flannery, B. P., *Numerical Recipes in FORTRAN. The Art of Scientific Computing*, Cambridge University Press, Cambridge, 1992.
 - [33] Bisnovatyi-Kogan, G. S. & Silich, S. A., Shock-wave propagation in the nonuniform interstellar medium, *Rev. Mod. Phys.* 67 (1995) 661.
 - [34] Dickey, J. M. & Lockman, F. J., H I in the Galaxy, *ARA&A* 28 (1990) 215.
 - [35] Lockman, F. J., The H I halo in the inner galaxy, *ApJ* 283 (1984) 90.
 - [36] McKee, C. F., Astrophysical shocks in diffuse gas, in: Dalgarno, A. & Layzer, D. (Eds.), *Spectroscopy of Astrophysical Plasmas*, 1987, pp. 226–254.
 - [37] Zaninetti, L., Evolution of superbubbles in a self-gravitating disc, *Monthly Notices of the Royal Astronomical Society* 425 (2012) 2343.
 - [38] Dyson, J. E. and Williams, D. A., *The Physics of the Interstellar Medium*, Institute of Physics Publishing, Bristol, UK, 1997.

-
- [39] Padmanabhan, P., *Theoretical Astrophysics. Vol. II: Stars and Stellar Systems*, Cambridge University Press, Cambridge, 2001.
- [40] Smith, N., Dissecting the Homunculus nebula around Eta Carinae with spatially resolved near-infrared spectroscopy, *MNRAS* 337 (2002) 1252.
- [41] Spitzer, Jr., L., The Dynamics of the Interstellar Medium. III. Galactic Distribution, *ApJ* 95 (1942) 329.
- [42] Rohlfs, K. (Ed.), *Lectures on Density Wave Theory*, Vol. 69 of Lecture Notes in Physics, Springer-Verlag, Berlin, 1977.
- [43] Bertin, G., *Dynamics of Galaxies*, Cambridge University Press, Cambridge, 2000.
- [44] Padmanabhan, P., *Theoretical Astrophysics. Vol. III: Galaxies and Cosmology*, Cambridge University Press, Cambridge, 2002.
- [45] Hill, C. J., Ueber die Integration logarithmisch-rationaler Differentiale, *J. Reine Angew. Math.* 3 (1828) 101.
- [46] Lewin, L., *Polylogarithms and Associated Functions*, North-Holland, New York, 1981.
- [47] Olver, F. W. J., Lozier, D. W., Boisvert, R. F., & Clark, C. W., *NIST Handbook of Mathematical Functions*, Cambridge University Press, Cambridge, 2010.
- [48] Kompaneets, A. S., A Point Explosion in an Inhomogeneous Atmosphere, *Soviet Phys. Dokl.* 5 (1960) 46.
- [49] Olano, C. A., The propagation of the shock wave from a strong explosion in a plane-parallel stratified medium: The Kompaneets approximation, *A&A* 506 (2009) 1215.
- [50] Tomisaka, K. & Ikeuchi, S., Evolution of superbubble driven by sequential supernova explosions in a plane-stratified gas distribution, *PASJ* 38 (1986) 697.
- [51] Stone, J. M. & Norman, M. L., ZEUS-2D: A radiation magnetohydrodynamics code for astrophysical flows in two space dimensions. I—The hydrodynamic algorithms and tests., *ApJS* 80 (1992) 753.
- [52] Wouterloot, J. G. A., Brand, J., Burton, W. B., & Kwee, K. K., IRAS sources beyond the solar circle. II—Distribution in the Galactic warp, *A&A* 230 (1990) 21.
- [53] Kim, K.-T. & Koo, B.-C., An Infrared and Radio Study of the Galactic Worm GW 46.4+5.5, *ApJ* 529 (2000) 229.
- [54] Igumenshchev, I. V., Tutukov, A. V., & Shustov, B. M., Shapes of Supernova Remnants, *Soviet Astronomy* 36 (1992) 241.
- [55] Koo, D. C. & et al., Deep Pencil-Beam Redshift Surveys as Probes of Large Scale Structures, in: *ASP Conf. Ser. 51: Observational Cosmology*, 1993, 112+.

-
- [56] Hartmann, D. & Burton, W. B., *Atlas of Galactic Neutral Hydrogen*, Cambridge University Press, Cambridge, 1997.
- [57] Perrot, C. A. & Grenier, I. A., 3D dynamical evolution of the interstellar gas in the Gould Belt, *A&A* 404 (2003) 519.
- [58] Zaninetti, L., Models of Diffusion of Galactic Cosmic Rays from Superbubbles, *International Journal of Modern Physics A* 22 (2007) 995.
- [59] Rybicki, G. & Lightman, A., *Radiative Processes in Astrophysics*, Wiley-Interscience, New York, 1991.
- [60] Hjellming, R. M., *Radio Stars in Galactic and Extragalactic Radio Astronomy*, Springer-Verlag, New York, 1988.
- [61] Lozinskaya, T. A., Moiseev, A. V., Podorvanyuk, N. Y., & Burenkov, A. N., Synchrotron superbubble in the galaxy IC 10: The ionized gas structure, kinematics, and emission spectrum, *Astronomy Letters* 34 (2008) 217.
- [62] Maddox, L. A., Williams, R. M., Dunne, B. C., & Chu, Y.-H., Nonthermal X-ray Emission in the N11 Superbubble in the Large Magellanic Cloud, *ApJ* 699 (2009) 911.
- [63] De Young, D. S., *The Physics of Extragalactic Radio Sources*, University of Chicago Press, Chicago, 2002.
- [64] Zaninetti, L., Scaling for the intensity of radiation in spherical and aspherical planetary nebulae, *MNRAS* 395 (2009) 667.
- [65] Gray, M. D., Matsuura, M., & Zijlstra, A. A., Radiation transfer in the cavity and shell of a planetary nebula, *MNRAS* 422 (2012) 955.
- [66] Opsenica, S. & Arbutina, B., Numerical Code for Fitting Radial Emission Profile of a Shell Supernova Remnant. Application, *Serbian Astronomical Journal* 183 (2011) 75.
- [67] Goldstein, H., Poole, C., & Safko, J., *Classical Mechanics*, Addison-Wesley, San Francisco, 2002.
- [68] Zaninetti, L., On the spherical-axial transition in supernova remnants, *Astrophysics and Space Science* 337 (2012) 581.